Harrington, R. M., Kwiatek, G., Moran, S. C. (2015): Self-similar rupture implied by scaling properties of volcanic earthquakes occurring during the 2004-2008 eruption of Mount St. Helens, Washington. - *Journal of Geophysical Research*, *120*, 7, pp. 4966—4982.

DOI: http://doi.org/10.1002/2014JB011744

AGU PUBLICATIONS

JGR

Journal of Geophysical Research: Solid Earth

RESEARCH ARTICLE
10.1002/2014JB011744

Key Points:
- Seismic events at Mount St. Helens exhibit self-similar scaling
- Some volcanic seismic sources may be stick-slip
- Low-frequency earthquakes are not a definitive indicator of fluids

Supporting Information:
- Supporting Information S1

Correspondence to:
R. M. Harrington,
rebecca.harrington@mcgill.ca

Citation:
Harrington, R. M., G. Kwiatek, and S. C. Moran (2015), Self-similar rupture implied by scaling properties of volcanic earthquakes occurring during the 2004-2008 eruption of Mount St. Helens, Washington, *J. Geophys. Res. Solid Earth*, *120*, 4966–4982, doi:10.1002/2014JB011744.

Received 31 OCT 2014
Accepted 27 APR 2015
Accepted article online 12 MAY 2015
Published online 2 JUL 2015

Self-similar rupture implied by scaling properties of volcanic earthquakes occurring during the 2004-2008 eruption of Mount St. Helens, Washington

Rebecca M. Harrington[1], Grzegorz Kwiatek[2], and Seth C. Moran[3]

[1]Earth and Planetary Sciences Department, McGill University, Montreal, Quebec, Canada, [2]GFZ, German Research Centre for Geosciences, Potsdam, Germany, [3]Cascades Volcano Observatory, U.S. Geological Survey, Vancouver, Washington, USA

Abstract We analyze a group of 6073 low-frequency earthquakes recorded during a week-long temporary deployment of broadband seismometers at distances of less than 3 km from the crater at Mount St. Helens in September of 2006. We estimate the seismic moment (M_0) and spectral corner frequency (f_0) using a spectral ratio approach for events with a high signal-to-noise (SNR) ratio that have a cross-correlation coefficient of 0.8 or greater with at least five other events. A cluster analysis of cross-correlation values indicates that the group of 421 events meeting the SNR and cross-correlation criteria forms eight event families that exhibit largely self-similar scaling. We estimate the M_0 and f_0 values of the 421 events and calculate their static stress drop and scaled energy (E_R/M_0) values. The estimated values suggest self-similar scaling within families, as well as between five of eight families (i.e., $M_0 \propto f_0^{-3}$ and $E_R/M_0 \propto$ constant). We speculate that differences in scaled energy values for the two families with variable scaling may result from a lack of resolution in the velocity model. The observation of self-similar scaling is the first of its kind for such a large group of low-frequency volcanic tectonic events occurring during a single active dome extrusion eruption.

1. Introduction

One of the scientific highlights of the 2004–2008 eruption of Mount St. Helens (MSH) is that it was remarkably seismogenic, producing several million discrete earthquakes over the course of the eruption [*Moran et al.*, 2008a]. These earthquakes occurred in association with the continuous eruption of a series of essentially solidified dacite lava spines [e.g., *Scott et al.*, 2008; *Vallance et al.*, 2008; *Pallister et al.*, 2013], accompanied by very low gas emission rates [*Gerlach et al.*, 2008] and only a half-dozen small phreatic explosions [*Moran et al.*, 2008b]. Despite the low gas content and relative absence of explosive behavior, the vast majority of these events were low frequency (LF) in nature, with dominant frequencies in the 1–5 Hz range [e.g., *Harrington and Brodsky*, 2007; *Moran et al.*, 2008a; *Waite et al.*, 2008; *Matoza and Chouet*, 2010]. Typically, LF events at volcanoes are thought to indicate fluid involvement, either through resonance of fluid-filled cracks or cavities [e.g., *Aki et al.*, 1977; *Chouet*, 1996; *Neuberg*, 2000] or oscillations due to fluid-driven flow [e.g., *Julian*, 1994; *Rust et al.*, 2008]. Certain attributes of the MSH LF events are consistent with these models, including all-down first motions observed on some of the larger events [*Waite et al.*, 2008; *Moran et al.*, 2008a], moment tensor inversions of several larger events that indicated primarily volumetric sources [*Waite et al.*, 2008], and the observation of infrasound pulses associated with a number of the LF events implying an implosive source [*Matoza et al.*, 2009]. However, the absence of appreciable gas content and explosions during the eruption, the ample evidence for brittle deformation within the extruded dacite spines [e.g., *Pallister et al.*, 2013], and the approximately parallel relationship between event rate and extrusion rate [*Iverson et al.*, 2006; *Moran et al.*, 2008a], provided rationale for scientists monitoring the eruption to also consider models that involved stick-slip motion [e.g., *Iverson et al.*, 2006; *Harrington and Brodsky*, 2007; *Moran et al.*, 2008a; *Thelen et al.*, 2008]. In such stick-slip models, the observed low frequencies and extended codas are explained either through unusual source mechanisms such as slow rupture [e.g., *Bean et al.*, 2014] or the scattering of higher-frequency seismic waves and trapping of lower frequency waves in highly attenuating near-surface layers [*Malone*, 1983; *Kedar et al.*, 1996; *Goto*, 1999; *Goldstein and Chouet*, 1994; *Bean et al.*, 2008; *Tuffen et al.*, 2008; *Kennedy et al.*, 2009].

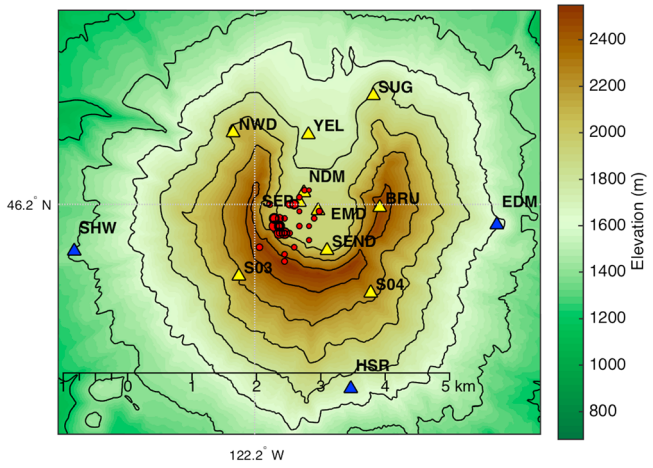

Figure 1. Station distribution and earthquake locations. Distribution of stations used in the analysis, and initial locations of earthquakes occurring during the temporary broadband deployment from 4 September 2006 to 9 September 2006. Yellow triangles indicate the 10 broadband stations used in the temporary deployment (Table 1). Blue triangles indicate permanent stations operated by the Pacific Northwest Seismographic Network (PNSN). Note that PNSN stations also operate at the same locations as the temporary stations installed at SEP, SUG, and YEL, but are not shown here, given that we use the higher sample-rate data from the temporary stations only. Blue stations were used for earthquake location only, as the SNR was not high enough for the earthquake spectral parameter estimation. Color scale indicates the elevation in meters.

A significant reason for why LF event mechanisms are still somewhat controversial is that it is difficult to obtain high-quality data recorded at stations close to the LF events [*Foulger et al.*, 2004; *Saccorotti et al.*, 2007]. In this paper, we attempt to address the question of LF source mechanisms at MSH by analyzing a unique data set recorded by the U.S. Geological Survey Cascades Volcano Observatory during a several week-long temporary deployment of 10 broadband seismometers in August and September of 2006, in the midst of the 2004–2008 eruption. The seismometers, located at distances of 0.2–2 km from the 2004 to 2008 vent, were deployed in part to improve location constraints and also to provide data useful for studying source mechanisms in greater detail. During the deployment, these instruments recorded thousands of LF events. The approach we follow in this paper is to examine the source scaling of these LF events, something that is not commonly done at volcanoes. *Galluzzo et al.* [2009] suggest scale-invariant stress-drop values for earthquakes on Mount Vesuvius; however, the number of events in their data set is observationally limited. A study by *Bean et al.* [2008] also suggests constant stress-drop scaling for simulations of low-frequency earthquakes at Mount Etna, and an additional study suggests similar scaling for a group of three volcanoes [*Bean et al.*, 2014]. In this paper, we will show observations of scale invariance based on the $M_0 - f_0$ and $E_R/M_0 - M_0$ scaling values obtained for a set of 421 events with high signal-to-noise ratios recorded during the temporary deployment at MSH. Such observations are the first of their kind for such a large number of volcanic seismic events from a single eruption and are facilitated by the high-quality data collected during the temporary deployment.

We start the paper by describing the waveform data used in our analysis in section 2, followed by a description of the methods used to perform double-difference relocations of the earthquakes and estimate the source spectral parameters (seismic moment and corner frequency) in section 3. Section 4 presents the results of our earthquake relocation calculations and the spectral parameter estimations followed by a discussion in section 5 of the scaling between corner frequency and moment, as well as the implications for our observations. Finally, we present our conclusions in section 6.

2. Data

The data used in this study originate from the period during a temporary deployment of 10 broadband seismometers that the U.S. Geological Survey's Cascades Volcano Observatory installed on the edifice of MSH from 4 through 9 of September 2006 where the highest number of stations were operational (Figure 1). One of the key aims of the deployment was to more precisely determine the location of the earthquakes associated with the dome extrusion. Five Guralp CMG-6TDs and five CMG-40Ts (paired with a RefTek RT130 digitizer)

Table 1. Seismic Station and Location Information for the Temporary Deployment From 4 Through 9 of September [a]

Station	Latitude (°N)	Longitude (°W)	Elevation (m)	Sampling Rate (sps)	Number of Correlated Events
BRU	46.1996	122.1747	2405	200	17
EMD	46.1991	122.1872	2135	200	27608
NDM	46.2016	122.1901	2074	200	24579
NWD	46.2100	122.2043	2121	200	21
S03	46.1899	122.2032	2265	200	196
S04	46.1876	122.1766	2230	200	411
SEND	46.1936	122.1854	2296	200	1325
SEP	46.2003	122.1910	2085	200	18269
SUG	46.2152	122.1761	1866	200	0
YEL	46.2098	122.1892	1729	100	0

[a]The stations listed in the table are those used for the source parameter analysis presented here, and are shown in yellow in Figure 1. The last column indicates the number of event pairs of the initial 6073 events found to have a maximum cross-correlation coefficient ≥ 0.8.

were installed at sites ranging from 0.2 to 2 km from the vent of the 2004–2008 eruption. All instruments had flat impulse responses in the frequency band of 0.033 Hz to the Nyquist frequency. The stations recorded continuously, with nine of the 10 recording at 200 sps (station YEL recorded at 100 sps). Table 1 lists the station locations and elevation information. Additional data come from permanent stations installed on the volcano edifice for the event location estimations, detailed below in the earthquake locations section.

We handpicked 6073 waveforms recorded on all 10 stations during the 6 day period when nine out of 10 stations were operational. The five stations closest to the vent (SEN, NDM, SEP, EMD, and YEL) were the primary stations that recorded the bulk of the picked waveforms at a high SNR. Station operation times varied over the 6 day period. For example, station SEP was the only consistently operating station from 4 September to 5 September. Stations EMD, NDM, and SEN recorded the events used in the analysis consistently from 6 September onward, with stations BRU, YEL, S03, S04, NWD, and SUG providing additional recordings for many of the same events (Figure 2).

The main objectives of this study are to obtain precise relocations of the low-frequency earthquakes that occurred during this 6 day time window to better pinpoint where in the crater they occurred, as well as to accurately estimate their source spectral parameters. Specifically, we determine the long-period spectral

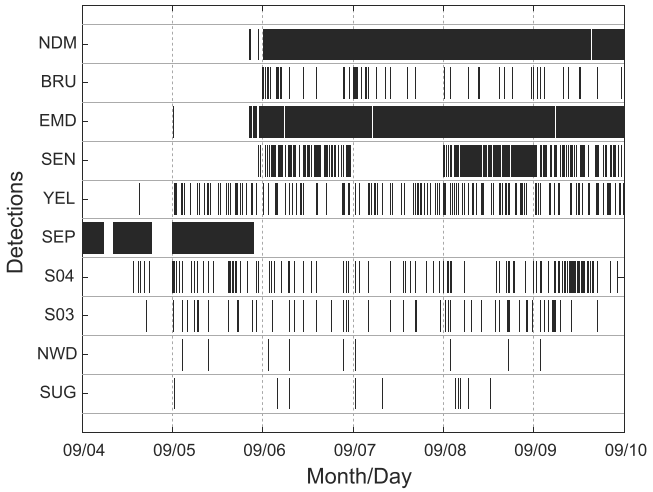

Figure 2. Station operation times during the temporary broadband deployment from 4 September 2006 to 9 September 2006. Stations EMD, NDM, and SEN recorded the events used in the analysis consistently from 6 September onward, with stations BRU, YEL, S03, S04, NWD, and SUG providing additional recordings for many of the same events.

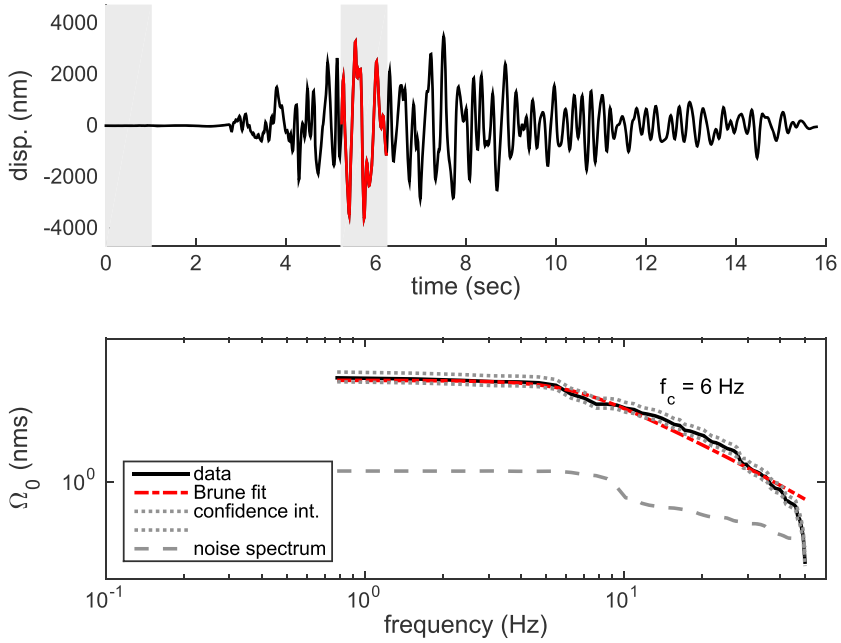

Figure 3. (top) Representative example earthquake (M_w 1.9) recorded on station YEL (vertical component shown) on 9 September 2006. The red part of the trace in the shaded background indicates the window used for the spectral calculation shown in Figure 3 (bottom), and the shaded area at the beginning of the trace shows the window used to calculate the noise spectrum in Figure 3 (bottom). (bottom) The event spectrum (solid black line) along with a least squares fit to a Brune spectral model (long dashed line in red) and the spectral confidence intervals (short dashed line) with estimated corner frequency of 6 Hz indicated in the top right corner. The spectrum was calculating using a multitaper method, and the errors shown indicate the 95% confidence interval calculated using a chi-squared approach.

amplitude (i.e., seismic moment) and the spectral corner frequency for the recorded events, and analyze their scaling relationship. We then calculate the stress drop and the seismically observable radiated energy from the values of seismic moment and corner frequency. Energy calculations vary widely, and are sensitive to corrections for attenuation [e.g., *Prejean and Ellsworth*, 2001; *Ide et al.*, 2003; *Venkataraman et al.*, 2006]. The strongly attenuating conditions in the volcanic edifice make correcting for nonsource-related effects a necessity [*Ide et al.*, 2003; *Harrington and Brodsky*, 2007; *Bean et al.*, 2008]. In our case, the seismicity occurring during the course of the deployment consisted of multiple event families sharing similar waveforms, suggesting that many of the events were colocated. Using the waveform similarity to infer event colocation thereby enables us to use spectral ratio methods to correct for travel path attenuation easily. For this reason, we select the events for our analysis from the original set of 6073 earthquakes based on whether the cross-correlation coefficient of one event with at least five other events exceeds a specified cutoff value of 0.8. We use the entire waveform to calculate the cross-correlation coefficient values, which is usually 10 s in length for most events.

In addition to enforcing a cross-correlation coefficient cutoff, we impose a SNR requirement for the data. We calculate the SNR by removing the instrument response and filtering the waveforms with a 4-pole, 2-pass Butterworth band-pass filter between 0.5 and 100 Hz. We use a filter bandpass of 0.5 to 50 Hz for station YEL, as it has a lower sample rate. We select time windows of 512 samples around the maximum amplitude of each event to calculate the signal amplitude, starting 64 samples before the peak amplitude (Figure 3). The reason for centering the window around the peak amplitude is that many earthquakes exhibit emergent arrivals, making precise determination of the event onset time difficult. We select a time window of 128 samples before the *P* wave onset time to calculate the noise window. (See Figure 3 for a representative earthquake waveform along with its spectrum). The vector sum (V) of both the signal and noise spectra from the three components is then calculated via

$$V_{\text{signal}}(f) = \sqrt{X^2_{\text{signal}} + Y^2_{\text{signal}} + Z^2_{\text{signal}}},$$
$$V_{\text{noise}}(f) = \sqrt{X^2_{\text{noise}} + Y^2_{\text{noise}} + Z^2_{\text{noise}}}. \quad (1)$$

We then calculate the power spectra following *Snoke* [1987] using V and the following equations,

$$J_{\text{signal}} = 2\int_0^\infty [V_{\text{signal}}(f)]^2 \mathrm{d}f,$$
$$J_{\text{noise}} = 2\int_0^\infty [V_{\text{noise}}(f)]^2 \mathrm{d}f. \tag{2}$$

The SNR of the power spectra is given by

$$\text{SNR} = 20\log_{10}(J_{\text{signal}}/J_{\text{noise}}). \tag{3}$$

We only use waveforms with SNR $\geq$ 20 in our analysis.

3. Methods

3.1. Earthquake Location and Magnitude Determination

The maximum moment magnitude value in our data set is M_w2.0, and many of the 6073 handpicked events are too small to be located. Of the 421 events fulfilling the SNR and cross-correlation criteria, only 107 earthquakes are large enough to record clear arrivals on at least six stations. We first compute starting locations using a 1-D velocity model [*Thelen et al.*, 2008] and then perform double-difference earthquake relocations of the 107 initial event locations using a 3-D velocity model [*Waite and Moran*, 2009], recovering an additional 15 events with relocated errors less than 500 m (horizontal and vertical errors). We term the 50 located (and 40 relocated) earthquakes "benchmark" events, using their estimated magnitude values to calibrate the remaining events using a spectral ratio technique that is detailed in the subsequent section. The following two sections describe the initial location and the double-difference relocation procedures.

3.1.1. Initial Locations

We use the open-source program Hypoellipse to determine the hypocenters of local earthquakes and their 68% confidence ellipsoids via a weighted regression [*Lahr*, 1999]. The advantage of using Hypoellipse for volcanic earthquakes is its ability to determine locations in areas of large topographic relief and to obtain hypocentral depth solutions that are permitted to be above the station elevations. Figure 1 denotes temporary and permanent stations from the Pacific Northwest Seismographic network in both yellow and blue triangles, respectively. We pick the *P* wave arrivals on all available recordings for the 107 events on both temporary and permanent stations (Figure 1), assigning a phase quality of 0–4 for each pick. Phase quality is defined by the timing uncertainties given in Table S1 in the supporting information, and we only use arrivals with quality of 2 or better for computing event locations. The phase quality weight codes correspond to the uncertainties in the phase arrival time and are listed in Table S1. Many of the events have emergent arrivals and often lack distinct *S* wave arrivals (Figure 3), but the expected similarity of *P* and *S* wave arrival times would likely obscure the *S* wave arrivals for the majority of events. For example, the *S-P* phase arrival times should be $\leq$ 0.8 s assuming a *P* wave velocity of 2.7 km/s and a Poissonian solid; therefore, we do not use *S* wave arrival picks in the earthquake location procedure.

The emergent character of many waveforms may be the result of the highly attenuating properties of the shallow volcanic edifice. The seismic record section of a representative event in Figure 4 demonstrates the attenuation effects on a seismogram over the travel path. The waveforms recorded on stations closest to the hypocenter show compact waveforms, while waveforms recorded on further stations show an apparent extended duration resulting from dispersion. Similarly, the filtered seismic record section shows the same dispersion effects in the frequency band between 0.05 and 5 Hz (Figure S3). Note that the dispersion effects can be recognized even for waveforms at stations with short hypocentral distances ($<$ 5 km). The more compact waveforms on stations closer to the source emphasizes that much of the extended apparent duration of the volcanic events may result from travel path rather than source effects.

In addition to the station and phase arrival information, Hypoellipse requires a velocity model as input. We use a merged velocity model consisting of the velocity profile provided in the appendix of *Thelen et al.* [2008] for the top 1.1 km and the profile provided in Table 1 of *Thelen et al.* [2008] at greater depths. The profile provided in the appendix results from a seismic experiment performed in 2005 aimed at improving the velocity model at shallow depths ($\leq$ 2 km) in the volcanic edifice. We tested the performance of the model in Table 1 of *Thelen et al.* [2008] without any modification against the merged model and found that the locations were similar, but

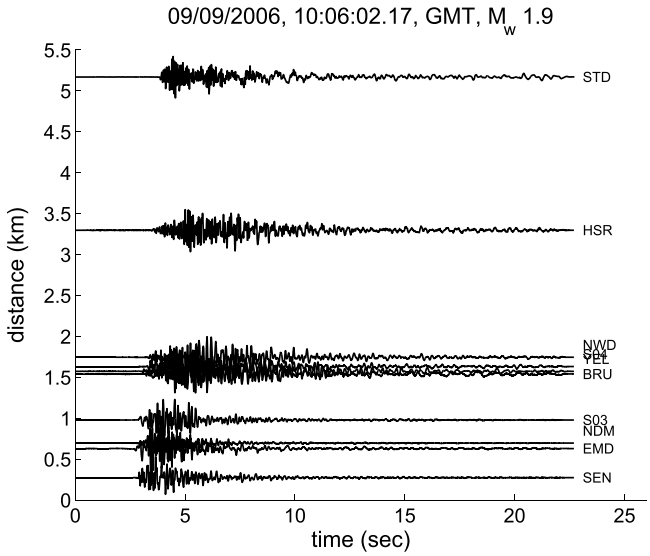

Figure 4. Example waveforms of a representative earthquake displayed in order of increasing distance of recording station from the hypocenter. Compact waveforms recorded at closer distances demonstrate the strong attenuation and dispersion effects along the travel path in the volcanic edifice. A filtered version of the record section is shown in Figure S3. Event shown has ID 0936359 (Table S2).

that the locations using the merged model showed slightly less scatter. We therefore use the merged model containing higher resolution in the shallower part of the edifice, given that most of the hypocentral depths are above 500 m (Table 2). Figures 5 and 6 show initial benchmark locations of the 35 events with horizontal location errors $\leq$ 1 km. Tables S2 and S3 in the supporting information list the locations, origin times, and location errors for the benchmark events within the 68% confidence limits, as well as the number of phase arrival picks used in the location calculation.

3.1.2. Double-Difference Relocations

The double-difference relocation program HypoDD uses initial earthquake locations together with cross correlation between earthquakes recorded on individual stations to calculate travel time differences between earthquakes with similar waveforms, which results in improved relative locations between events. It is an iterative least squares procedure that relates residuals between the observed and predicted phase travel time differences for pairs of earthquakes observed at common stations to changes in the vector connecting their hypocenters [*Waldhauser and Ellsworth*, 2000]. The most current release of HypoDD is based on the version 1.0 developed by *Waldhauser* [2001], and it allows for the input of a 3-D velocity model, as well as station elevation information. We perform the relocation calculation of the initial 107 located events using the 3-D velocity model of *Waite and Moran* [2009]. We initially retain all 107 events in an effort to increase the number of benchmark locations beyond the original 35 events through possible reduction of errors following relocation.

Table 2. Velocity Model Used in This Study, Taken From Table 1 and the Appendix of *Thelen et al.* [2008]

P Wave Velocity (km/s)	Depth (km)	*P*/*S* Wave Velocity Ratio
2.66	0.0	1.79
3.48	0.5	1.78
4.3	0.8	1.78
5.12	1.1	1.78
6.0	3.9	1.78
6.2	6.5	1.73
6.6	10.5	1.73
6.8	18.5	1.73
7.1	34.5	1.73
7.8	43.5	1.73

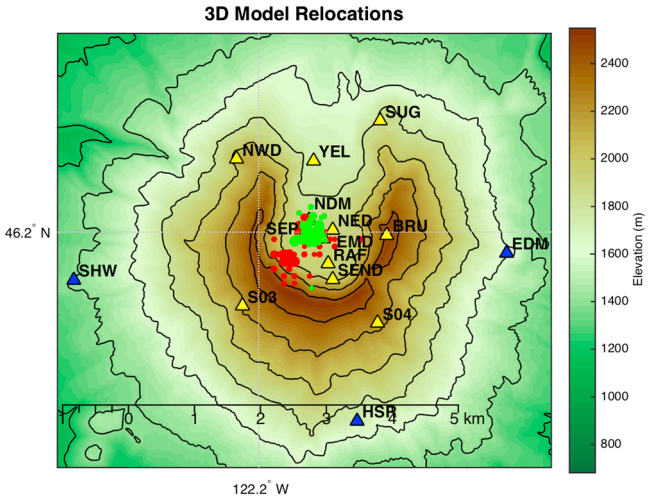

Figure 5. Original hypocenters (red) and double-difference relocations (green) using a centroid start location for relocation. Stations from the temporary deployment in 2006 are shown in yellow, permanent PNSN stations are shown in blue. Initial locations (red) have location errors of less than 1 km, and relocations (green) have location errors less than 500 m. All events and location uncertainties shown are listed in Tables S4 and S5. There are 35 initial locations, and 27 double-difference relocations, 15 of which are not included in the list initial locations with errors less than 1 km (see text).

HypoDD allows for variation of many input parameters, such as minimum and maximum allowable earthquake source/recording station distance, the minimum allowable number of links between neighboring events to be relocated, and the weighting between cross-correlation results. We found that after selecting reasonable distance cutoffs based on our station geometry, our results varied little when changing the parameters controlling the number of iterations and the weighting for cross correlated and catalog travel time differences. Figure 5 shows the earthquake relocation results (green dots) relative to the original catalog locations (red dots) for a centroid initial starting location, and Figure S1 shows the 90% error ellipses based on a random replacement bootstrap sampling approach. We replace the final residuals from the relocated hypocenters by samples drawn with replacement from the observed residual distribution and relocate all events with the bootstrap sample data, following the approach used by *Waldhauser and Ellsworth* [2000]. We repeat the procedure 200 times and calculate the error ellipses based on the distribution of locations from

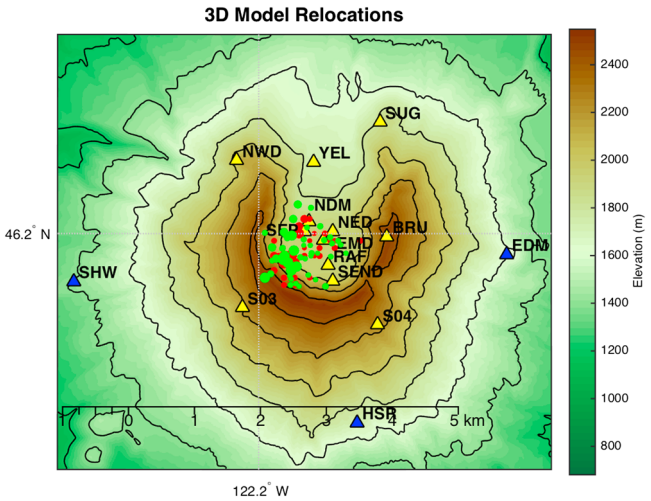

Figure 6. Original hypocenters (red) and double-difference relocations (green) using catalog starting locations. Stations from the temporary deployment in 2006 are shown in yellow, permanent PNSN stations are shown in blue. Initial locations (red) have location errors of less than 1 km, and relocations (green) have location errors less than 500 m. All events shown are listed in Tables S4 and S5. There are 35 initial locations, and 40 double-difference relocations, 15 of which are not included in the list initial locations with errors less than 1 km (see text).

the 200 relocation calculations. We weight stations EMD, NDM, RAFT, SEND, and S03 with unit weights due to their significantly higher SNR quality, and weight all other stations at 50%. Relocation results are listed in Tables S4 and S5 in the supporting information.

3.2. Spectral Parameter Estimation

The complex travel path of seismic waves in a volcanic edifice and the extent of damage in the host rock can make intrinsic and travel path attenuation, as well as local site effects, in a volcanic environment more pronounced than a typical tectonic setting, particularly at high frequencies [*Lacruz et al.*, 2009; *Petrosino et al.*, 2002; *Gudmundsson et al.*, 2004; *Bean et al.*, 2008]. The small magnitude of events contained in our data set implies that the frequency band of importance to the analysis is $\geq$1Hz, based on expected corner frequency values for the magnitudes and seismic wave velocities considered [cf. *Kwiatek et al.*, 2011, Figure 8]. In order to check that we do not miss any low-frequency energy below 1 Hz, we initially check the displacement spectra of the raw waveforms over the frequency range where the instrument response is flat (30 s – 100 Hz). The event waveforms all show flat displacement spectra up to the corner frequency, suggesting no additional energy in the low frequencies.

The main goal of our analysis is to accurately estimate the seismic moment and spectral corner frequencies of the group of low-frequency volcanic earthquakes in order to get the best possible estimates of source parameters such as static stress drop and seismic energy radiated per unit size. *Anderson* [1986] suggests that improperly correcting for seismic attenuation may lead to underestimation of spectral corner frequencies and ultimately to poor estimations of source scaling. An accurate correction for attenuation is, therefore, necessary for reliable corner frequency estimation. Spectral ratio methods are a powerful tool for correcting for attenuation and site effects when one has the advantage of having many colocated events with a range of sizes, as is the case for our data set [e.g., *Ide et al.*, 2003; *Prieto et al.*, 2004; *Abercrombie and Rice*, 2005; *Imanishi and Ellsworth*, 2006; *Harrington and Brodsky*, 2007; *Baltay et al.*, 2011; *Kwiatek et al.*, 2011, 2014].

Subjecting the initial set of 6073 events to the cross correlation and SNR criteria discussed previously leaves us with 421 events for spectral ratio analysis. The cross-correlation criterion only requires that an earthquake has similar waveforms to at least five other earthquakes, so we must first categorize the earthquakes into event families. We perform a cluster analysis using cross-correlation coefficient as a measure of similarity between events. We generate a dendrogram plot and organize 421 events into eight families, where each family contains at least one benchmark event with a catalog magnitude. Using the locations of the benchmarks within a family, we can infer the locations of the remaining events by assuming that the benchmark with which an event shares the highest cross-correlation coefficient is collocated with the smaller, unlocated event.

Once we determine families, we use the spectral ratio approach to estimate the long-period spectral amplitude and the corner frequency of all events. The method is largely based on those presented in *Kwiatek et al.* [2014] and consists of two major stages that are performed separately for each family. In the first stage, we estimate the seismic moment and corner frequency (M_0, f_0) of all seismic events using standard source parameter estimation methods to calculate the a priori values for input into the spectral ratio inversion. In the second stage, the spectral ratio inversion refines the starting moment and corner frequency values using the stations with the highest SNR waveform recordings: EMD, NDM, and SEND.

The source parameter estimation in the first stage consists of determining M_0, f_0, and quality factor Q_0 of each benchmark event using a standard fitting method [*Kwiatek et al.*, 2011, 2014]. We assume that an individual earthquake source can be described by a Brune's spectral model [*Brune*, 1970, 1971] where the ground velocity spectrum measured at a given station can be written as

$$\dot{u}_c(f) = \frac{\langle U_{\phi\theta} \rangle}{4\pi\rho c^3 R} \frac{2\pi f M_0}{1 + (f/f_0)^2} \exp\left(\frac{-\pi R f}{c Q_c}\right). \quad (4)$$

The variable $\rho = 2500\,\mathrm{kg/m^3}$ represents the rock density, c represents the seismic velocity (α or β for P or S waves, respectively), $\langle U_{\phi\theta} \rangle$ represents the radiation pattern correction coefficient, and Q_c is the path averaged P or S wave quality factor [*Boatwright*, 1980; *Abercrombie*, 1995; *Aki and Richards*, 2002]. As the shear waves likely comprise the highest amplitude signal in our seismograms, we assumed $c = \beta = 1500\,\mathrm{m/s}$ and average S wave radiation pattern correction coefficient $\langle U_{\phi\theta} \rangle = 0.63$ [*Boore and Boatwright*, 1984], and $Q_c \approx Q_\beta$. We invert for the M_0, f_0, and Q_0 by optimizing the cost function $\left\| \log(\dot{u}(f)) - \log(\dot{u}_{\mathrm{obs}}(f)) \right\|_{L_1} = \min$. [cf. *Kwiatek et al.*, 2011, 2014]. The optimization results in consistent attenuation estimates among all benchmark events, with an average value of $\overline{Q_\beta}$=15.

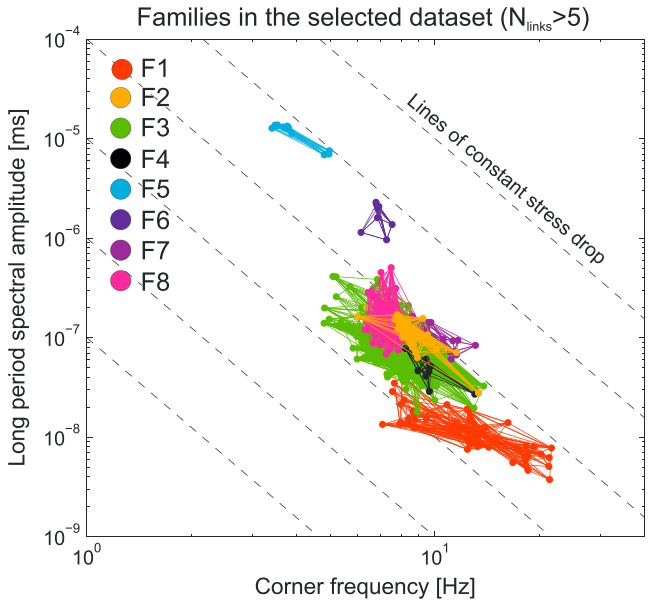

Figure 7. Subset of 421 events satisfying the cross-correlation criterion imposed for the spectral ratio analysis (see text). The figure shows the long-period spectral amplitude and corner frequency values, and demonstrates that the corner frequencies are within the bandwidth of high SNR. Interestingly, we also get an idea of the constant stress-drop scaling even before performing the spectral ratio inversion to obtain more accurate corner frequencies. The color code indicates the clustering into event families based on cross-correlation values. Each family contains a benchmark (cataloged) event, with the exception of family 1, so we have assumed that family 1 is located in the mean location of all other families. Even without applying the spectral ratio technique to correct for attenuation, and assuming similar locations for family 1, the scaling of the long-period spectral amplitude with f_0 suggests self-similarity. We do not indicate stress-drop values, as we do not have robust locations and, therefore, have only poor constraints on seismic moment for family 1.

To obtain starting M_0 and f_0 values for nonlocated events, we first calculate the raw long-period spectral amplitude Ω_0 and corner frequency f_0 values using ground velocity and ground displacement spectra following Snoke's method (see equations (3)–(11) in *Snoke* [1987]). Figure 7 shows the initial Ω_0 and f_0 values. The f_0 values range from approximately 3–30Hz and lie well within the band of high SNR. Interestingly, in a rough sense, the figure suggests that without any attenuation correction, the scaling between size and duration resembles constant stress-drop scaling behavior ($\Omega_0 \propto f_0^{-3}$). We then correct the spectra for average attenuation $\overline{Q_\beta}$ estimated from benchmark events, resulting in higher f_0 estimates. Finally, we estimate the starting value of seismic moment M_0 of each nonbenchmark event by using the standard relation $M_0 = 4\pi\rho\beta^3 R\Omega_0/\langle U_{\phi\theta}\rangle$ assuming proximity to a benchmark with a known location and using the average radiation pattern coefficient correction for S waves $U_{\phi\theta} = 0.63$ [*Boore and Boatwright*, 1984].

Once we calculate the input parameters (M_0, f_0), we proceed to the second stage of the method which uses a spectral ratio inversion to refine the values for the nonbenchmark events. The spectral ratio technique suppresses all nonsource-related effects from the earthquake waveform, such as instrument response, site response, travel path effects, so that the spectral corner frequency can be more accurately estimated from the earthquake source spectrum. To estimate source parameters from spectral ratio pair, the two events comprising the pair must have similar focal mechanisms and rupture complexity, and must be nearly colocated, meaning that the source-receiver travel path must be nearly identical. The high cross-correlation coefficients of the pairs used in the inversion (≥ 0.8) suggest that the focal mechanism and location constraints are satisfied.

The following is an analytical expression of the spectral ratio of two events i and j (where $i \neq j$):

$$\Psi^{ij}(f) = \frac{\dot{u}^i(f)}{\dot{u}^j(f)} = \frac{M_0^i\left[1+(f/f_0^j)^2\right]}{M_0^j\left[1+(f/f_0^i)^2\right]}. \quad (5)$$

If we then measure the spectral ratio (Ψ^{ijk}) directly from the seismic data using the ground velocity spectra measured at station k, we can compute the difference between the theoretical value and the measured value.

Summing the differences over all events i, j, and all stations k in a given family A, we define the following cost function:

$$\epsilon\left(\mathbf{f_0}, \mathbf{M_0}\right) = \sum_k \sum_{(i,j)\in A} w_{ij} \left\| \log \Psi^{ij}(f) - \log \Psi^{ijk}(f) \right\|_{L_1}, \tag{6}$$

where w_{ij} are weights equal to the cross-correlation value between each event pair. We use a Monte Carlo-based Metropolis-Hastings Random Walk (MHRW) algorithm to estimate the M_0 and f_0 of nonbenchmark events in order to evaluate probability density functions of their source parameters [*Mosegaard and Tarantola*, 1995; *Metropolis et al.*, 1953; *Hastings*, 1970].

The entire procedure works as follows: first, we calculate the cost function in equation (6) using the starting M_0 and f_0 values calculated in the first stage. We then slightly perturb the source parameters of nonbenchmark events and recalculate the cost function. If the new value is smaller than the original value, the new model is accepted. If the new value of the cost function is larger than the original, then the model is either accepted or rejected with a predetermined probability. For example, the likelihood function L defined as

$$L\left(\mathbf{f_0}, \mathbf{M_0}\right) = \exp\left(-\frac{\Delta\epsilon\left(\mathbf{f_0}, \mathbf{M_0}\right)}{T}\right), \tag{7}$$

where T is a constant referred to as temperature, and $\Delta\epsilon\left(\mathbf{f_0}, \mathbf{M_0}\right)$ is a change in the cost function value in one step of MHRW algorithm. If L exceeds a randomly drawn number ranging between 0 and 1, then the new model is accepted according to the Metropolis rule [*Hastings*, 1970; *Mosegaard and Tarantola*, 1995]. The constant T determines the acceptance rate for cases where the error function of the new model exceeds the error function of the previous model. We determine our T value by trial and error to correspond to a 50% acceptance rate. The advantage of not rejecting all cases where the value L increases is that it prevents the inversion from converging on a local minimum.

Initially, the cost function changes rapidly with each sampling as the source parameters converge on fixed values. We typically perform 100,000 sampling iterations in the $(\mathbf{M_0}, \mathbf{f_0})$ parameter space. We performed 500,000 iterations for family 3, which contains the largest number of events. Typically after approximately 20,000 iterations, the source parameters start to oscillate around fixed values. The collection of models obtained after stability has been reached has a frequency distribution proportional to the a posteriori distribution in the model space [*Mosegaard and Tarantola*, 1995]. Events for which the inversion reaches a stable solution presents a Gaussian marginal probability distribution of model parameters in $\log_{10}$ space of $(\mathbf{M_0}, \mathbf{f_0})$, where the values are assumed to contain statistically independent, random errors [*Mosegaard and Tarantola*, 1995]. We take the mean of the 2-D Gaussian marginal distributions as the final values for the estimation of M_0 and f_0 for each event. We reject events having a skewed (i.e., non-Gaussian) distribution of model parameters as unstable solutions.

4. Results

4.1. Earthquake Relocations

The relocation results vary when using catalog location values versus cluster centroid starting values. The primary reason for the difference is the close source station distances for some clusters and the requirement that the cluster station distance be much greater than the distance between events. Figure 6 shows the same relocations as shown in Figure 5 with all parameters identical except for the catalog starting values. Figure S2 shows the 90% error ellipses for the catalog starting values. Given that the double-difference relocation method provides more accurate relative locations between events than it does accurate absolute locations, we show the second set of locations for completeness. Based on the station configuration, the number of events, and the resolution of the velocity model at shallow depths, it is difficult to constrain whether the cluster of events in the southwest portion of the crater in Figure 6 is located there, or further to the Northwest, as is depicted in Figure 5. The negligible differences between the moment values calculated using the initial locations versus the relocations suggest that the differences in absolute locations have little bearing on the source scaling results, which we discuss below. However, the higher number of relocated events with errors less than 500 m with catalog starting locations relative to cluster centroid starting locations, 40 events versus 27, seems to suggest that the catalog starting position results are more accurate. One thing to note is that even when considering the results obtained with catalog starting values as the favorable, it still places the majority of the 421 events analyzed as occurring directly under the crater. Figures 5, 6, and 8 show that the

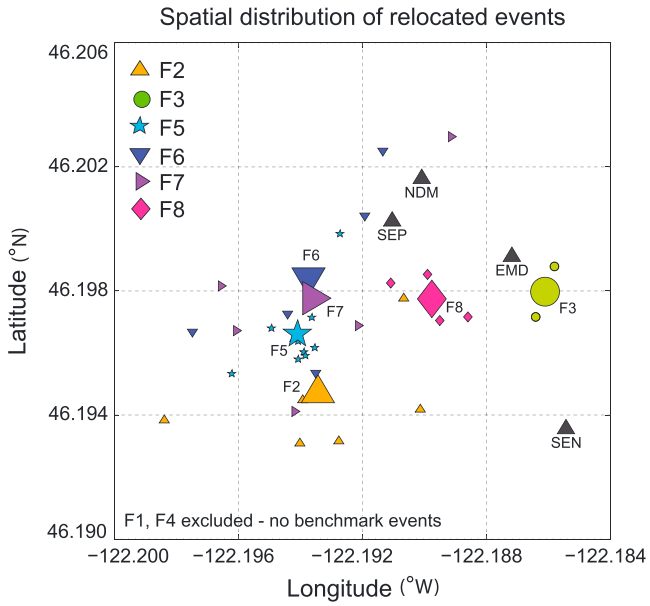

Figure 8. Benchmark locations of relocated earthquakes (based on catalog starting positions) for event families with source parameters estimated in the spectral ratio inversion (9. Color-coded symbols represent the families determined by a cluster analysis of cross-correlation coefficients. Small symbols represent the individual benchmark earthquake locations; larger symbols indicate the average benchmark location for each family.

largest family containing the majority of events, family 3, has benchmarks that locate near the vent, regardless of starting value. The lower error values obtained using catalog starting values are the only metric with which we can set a preference for the relocations shown in Figure 6. We therefore present the moment corner frequency scaling and moment versus scaled energy figures based on the relocations calculated using catalog starting values.

4.2. Earthquake Source Spectra

The scaling of M_0 and f_0 values obtained via the spectral ratio inversion follows lines of constant stress drop within families, as well as between most families, excluding family 8 (Figure 9). We calculate lines of constant stress drop using the expression for the static stress drop on a circular crack, namely,

$$\Delta\sigma = \frac{7}{16} M_0 \left(\frac{2\pi f_0}{1.32\beta} \right)^3, \tag{8}$$

using a shear wave velocity of β =1500 m/s and the constant k = 1.32 relating the fault radius to the corner frequency [*Eshelby*, 1957; *Madariaga*, 1976]. The value of β = 1500 m/s results from the compressional wave speed (α) in the top layer of the volcanic edifice (see Table 2) and the assumption of a Poisson solid (i.e., $\beta = \alpha/\sqrt{3}$). The estimated shear speed in the edifice may be an overestimate for the shallowest layers, and there is likely a significant degree of variability corresponding to variability in rock density. The discussion below details, in fact, why the observation may be consistent with the value β = 1500 m/s being an overestimate. A comparison of the spectral ratio inversion results with our starting values of M_0 and f_0 measured directly from the spectra shows that the estimated f_0 values increase for the events with $M_w < 1.5$ as we would expect once attenuation has been accounted for (Figure 7). The f_0 values for the three events with the smallest magnitude values in family 5 increase by a significant amount, corresponding to the highest stress-drop values for all events (~5 MPa). However, the stress-drop values for the three events should be considered with caution. We speculate that their estimated corner frequency values are the least reliable of the estimated f_0 values for all events, because they have the lowest cross-correlation values with their respective group of benchmark events (values of 0.8), suggesting that the source-receiver paths are less similar relative to other event pairs. The low cross-correlation values together with the high estimated f_0 values suggest that the starting f_0 values could be a better estimation of the true values for the three outliers in family 5.

The M_0-f_0 scaling between families 2, 3, 5, 6, and 7 suggests constant stress-drop scaling, where $M_0 \propto f_0^{-3}$ for the volcanic earthquakes occurring during the study period. Note that family 4 based on the initial

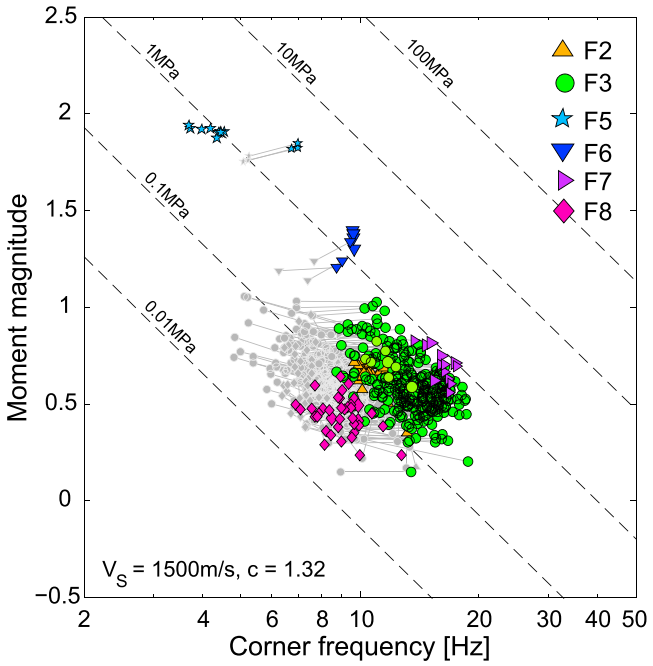

Figure 9. M_0 and f_0 values estimated from the spectral ratio inversion of relocated earthquakes using catalog starting locations. (Similar plots based on initial locations and centroid starting locations show negligible differences). Note that events originally in family 4 were grouped with family 3 based on the stability of the spectral ratio inversion results with the new benchmarks determined with hypocenter relocations. Color-coded symbols represent the families determined by a cluster analysis of cross-correlation coefficients. Figure 7 shows the starting values for the inversion (shown as grey dots connected to the new values with a line). Note that the events of Family 1 shown in Figure 7 have no benchmark with which absolute M_0 values could be estimated and are not included in the inversion. Dashed lines represent lines of constant stress drop calculated using a shear wave velocity of β = 1500 m/s (where $\beta = \alpha/\sqrt{3}$ for the top layer in Table 2) and c = 1.32, where c is the constant relating fault radius and f_0 [*Madariaga*, 1976]. Lower f_0 values for family 8 compared to the remaining families may result from a lack of resolution in the velocity model (see discussion in text).

benchmarks is grouped with family 3 based on the new set of benchmarks recovered with the earthquake relocations. Static stress-drop values range between 0.1 and 1 MPa, excluding the three outliers in families 5 and 8, and are within the range of values observed for earthquakes in tectonic settings [e.g., *Abercrombie*, 1995; *Prieto et al.*, 2004; *Abercrombie and Rice*, 2005; *Shearer et al.*, 2006; *Allmann and Shearer*, 2007; *Harrington and Brodsky*, 2009; *Baltay et al.*, 2011; *Kwiatek et al.*, 2011]. The stress-drop values for family 8 range between 0.02 and 0.1 MPa, and are smaller than the 0.1 MPa lower bound observed by other studies. The lower f_0 and stress-drop values in family 8 may actually be explained by spatial variations in the seismic velocities within the volcanic edifice. *Allmann and Shearer* [2007] show that stress drop can be underestimated if seismic shear wave velocities are overestimated, producing an apparent variation in stress drop that is not real for broad areas where seismic velocity is erroneously assumed constant. If the earthquakes in family 8 occurred in rock with locally lower seismic shear wave velocity, then the values in Figure 9 could be an underestimate. It is also possible that the stress drops for family 8 are indeed lower, due to the earthquakes rupturing in very soft/broken rocks at a lower rupture velocity [e.g., *Bean et al.*, 2014]. The M_0-f_0 scaling within family 8 also does not rule out self-similarity; however, the small range of magnitudes prohibits any conclusions about scaling.

5. Discussion

The constant stress-drop scaling observed for the earthquakes studied here strongly suggests that they are finite-duration slip events on fault planes. As mentioned above, the moment values do not change significantly when using centroid versus catalog starting values for the relocation, and the scaling persists regardless of starting values. While moment tensor inversions in theory might provide valuable information on the source mechanics of these events, the shallow depths and the volcanic setting in which events occur make the data set particularly ill suited to such methods. *Bean et al.* [2008] show that the low velocities in the shallow layers of a volcano coupled with the topography lead to spurious and unstable solutions of moment tensor

inversions. Alternatively, one can show by theoretical considerations that the expected duration for a mode II shear displacement on a crack will produce a moment and corner frequency scaling $M_0 \propto f_0^{-3}$ for constant stress drop [e.g., *Ide et al.*, 2003]. Even if the displacement on the crack is more similar to mode I or III failure, one would still expect to see a scaling relationship. If an alternative mechanism to fault slip better describes the source process of these events, such as the coupling of turbulent fluid flow to the walls of a crack in an elastic medium as the result of a pressure differential on two sides of a crack, then we would expect a distinct lack of scaling between corner frequency (i.e., duration) and size (moment). In any model involving fluids as the source of seismic waves, the duration of the event is dependent on the pressure difference on either side of the crack, and there would be no specific dependence on size [*Julian*, 1994].

The earthquakes in our study occurred within the actively deforming volcanic dome, a highly heterogeneous environment consisting of, among other materials, crystalline dacite spines, broken up spine material, rock debris, gouge, ash, and glacier ice, all with varying material properties and seismic velocities [*Herriott et al.*, 2008; *Vallance et al.*, 2008]. To assume a constant velocity within the top layer of the volcanic edifice is an oversimplification; however, we are limited by the constraints of the highest resolution velocity model [*Thelen et al.*, 2008; *Waite and Moran*, 2009]. Some of the differences in estimated f_0 and static stress-drop values may therefore result from an erroneous assumption of a constant shear wave velocity within the upper layers, rather than actual differences in the values themselves. The lower stress-drop values may indeed be real, but there is no compelling evidence of any localized changes in lithology that would change rupture velocity significantly, and thus stress drop, without seeing corresponding characteristic differences in the waveforms between families. Furthermore, the spectral ratio versus corner frequency estimation before events are calculated suggests that stress-drop values in family 8 might not be that different (Figure 7). Therefore, variations in rock textures in the crater that cause variations in seismic velocity as discussed above may offer a more simple explanation for the varying stress-drop values.

One can understand the f_0 dependence on seismic velocity values by considering the physical interpretation of the spectral corner frequency. What we measure when estimating the spectral corner frequency for a given earthquake is the duration of rupture (τ), where $f_0 \propto 1/\tau$ [*Madariaga*, 1976; *Beresnev*, 2002; *Kanamori and Brodsky*, 2004]. The rupture velocity (V_r) determines how long it takes for the rupture to travel the length of the fault radius (r), and therefore also determines the rupture duration. Rupture velocity is limited by the Rayleigh wave velocity for subshear rupture speeds, suggesting that rupture velocity is some fraction of the shear wave speed. Although observations suggest a wide range of values, typical values for shallow earthquakes range from $V_r \approx (0.6–0.9)\beta$ [*Freund*, 1979; *Imanishi et al.*, 2004; *Kanamori and Brodsky*, 2004; *Yamada et al.*, 2005a, 2005b; *Tomic et al.*, 2006; *Dreger et al.*, 2007]. Therefore, if $f_0 \propto 1/\tau$ and $\tau = r/V_r$, it follows that f_0 is proportional to the shear wave velocity, assuming that rise time is significantly shorter than rupture time [*Heaton*, 1990]. Errors in estimating the shear wave velocities could then translate to systematic errors in the corner frequency values. Considering the highly heterogeneous structure of the volcanic dome, it follows that assuming a constant β value for all earthquakes may lead to systematic errors in the observed f_0 values between families, depending on where the families occur.

Figure 8 shows that with the exception of family 3, all families with higher f_0 values (families 2, 5, 6, and 7) have average locations more tightly clustered together to the east of families 3 and 8. If family 8 occurs in more damaged rock, then the β values near their source regions would be lower than the constant β value assumed, and the f_0 would also be lower than observed for other families. For example, assuming a value of $\beta = 1500$ m/s, a M_w 0.5 earthquake with a static stress-drop value of 0.5 MPa would have a corner frequency value of 17 Hz; the same earthquake would have a corner frequency value of 11 Hz assuming $\beta = 1000$ m/s (equation (8)). Such differences in β would easily explain the differences in observed f_0 values between family 3 and family 8. However, due to a lack of resolution in the velocity model and the errors in earthquake locations, we do not try to draw any extensive conclusions regarding the relationship of f_0 values and location. We merely use the benchmark location map as a consistency check on the plausibility of the variation in f_0 values for family 8 resulting from variations in the β values throughout the dome.

The static stress-drop values calculated using the Brune model and the f_0 values are also proportional to the seismically radiated energy per unit moment, or the apparent stress, when multiplied by the shear modulus. We refer to the energy-moment ratio as the scaled energy here (E_R/M_0). One can obtain an analytical expression for the energy (or scaled energy) assuming an omega square source spectral model following *Ide and Beroza* [2001] [*Haskell*, 1964, 1966; *Aki*, 1967]. *Ide and Beroza* [2001] show that radiated seismic energy values

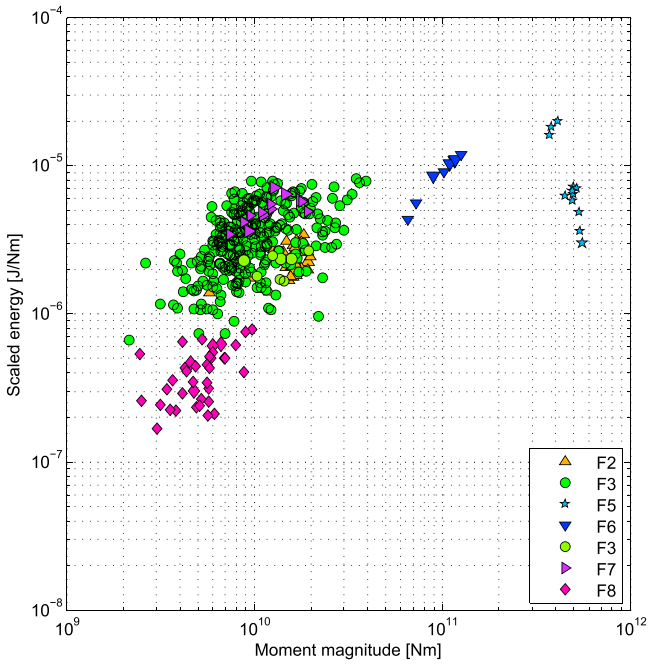

Figure 10. Seismically radiated energy per unit moment (scaled energy, E_R/M_0) values estimated from the spectral ratio inversion. The figure shows earthquakes relocated using catalog starting values but has negligible differences to earthquakes using centroid starting values or the original locations. Color-coded symbols represent the families determined by a cluster analysis of cross-correlation coefficients. Similar to Figure 9, events from families 2, 3, 5, 6, and 7 exhibit self-similar scaling with energy ratios ranging from 10^{-6} to 10^{-5}. Scaling for the events in family 8 remains ambiguous due to the small range of magnitudes. The difference in energy ratios between family 8 and the remaining groups may result from a lack of resolution in the velocity model (see discussion in text).

are often underestimated due to spectral integration over a limited bandwidth. They suggest that radiated energy may be better estimated by integrating the power spectral density of an omega square source spectral model from zero to infinite frequency, given that the integral has a closed form. Following *Ide and Beroza* [2001], the analytical expression for the radiated energy in terms of the moment and corner frequency is

$$E_R = \frac{\pi^2}{5\rho\beta^5} M_0^2 f_0^3 \tag{9}$$

(see Appendix A for the derivation). A comparison of equations (8) and (9) indicates that $E_R/M_0 \propto \Delta\sigma$. Therefore, constant static stress-drop values for a given set of earthquakes also imply constant scaled energy values. We calculate the scaled energy values presented here using equation (9). Equation (9) is independent of geometrical spreading and attenuation, and is therefore appropriate for source time spectra. Figure 10 shows the scaled energy values calculated using the M_0 and f_0 values in Figure 9. As one might infer from the lines of constant stress drop shown in Figure 9, families 2, 3, 5, 6, and 7 exhibit self-similar scaling. Family 8 exhibits lower scaled energy values, a direct result of the lower f_0 values (equation (9)). Again, we speculate that the lower energy values calculated for family 8 may result from a lack of resolution in the velocity model. Nevertheless, the scaled energy values for the majority of the events (families 2, 3, 5, 6, and 7) remain constant for nearly 2 orders of magnitude and exhibit similar values to those observed for tectonic earthquakes [e.g., *Abercrombie*, 1995; *Prieto et al.*, 2004; *Abercrombie and Rice*, 2005; *Imanishi and Ellsworth*, 2006].

6. Conclusions

In this paper, we have presented results from a relatively new approach (scaling analysis) to addressing the question of the source process involved in producing the millions of LF events associated with the MSH 2004–2008 eruption. We apply this approach to a unique data set recorded by 10 broadband stations deployed for several weeks at distances of 0.2–2 km from the vent. Of the 6073 manually detected events, we calculate double-difference relocations for 40 benchmark events that were recorded on at least six of the temporary stations and that also had epicentral location errors of less than 1 km. The 40 benchmark events

exhibited similar waveforms to an additional 381 earthquakes also with high signal-to-noise ratio recorded on fewer than six stations, comprising a total of 421 events used in our study. Using a clustering algorithm, we organize the 421 events into seven families and calculate the seismic moment and corner frequency values using a spectral ratio approach. The seismic moment and corner frequency values provide a size-duration relationship with which we calculate the static stress drop, and the proportion of seismically radiated energy per unit seismic moment, or scaled energy. Earthquakes from five of the seven families exhibit a relationship of $M_0 \propto f_0^{-3}$ and approximately constant scaled energy values for the volcanic earthquakes, which are similar to scaling relationships observed for standard tectonic events. Earthquakes from the remaining families do not have a wide enough range of magnitudes to draw conclusions about scaling but exhibit lower scaled energy values compared to the other families. The lower scaled energy values might be an artifact of neglecting velocity heterogeneities in the volcanic dome. The novel observation of self-similar scaling (i.e., $M_0 \propto f_0^{-3}$, or $E_R/M_0 \propto$ constant) for a group of relocated LF events at a volcano is similar to that observed by *Harrington and Brodsky* [2007] and is one of the first of its kind for such a large number of events from a single eruption, due to the unique station coverage. The observations are facilitated by the dense azimuthal station coverage with short source-receiver distances and suggest that some earthquakes in a volcanic environment behave much like their tectonic counterparts, despite their unusual waveform characteristics.

Appendix A: Analytical Expression for Radiated Energy

Following *Ide and Beroza* [2001], we rederive the analytical expression for E_R here leading to the expression for radiated energy given in equation (9). Equation (1) of *Ide and Beroza*, 2001 is the expression for a velocity spectrum measured at a given station based on a Brune spectral model

$$\hat{u}(f) = \frac{\Omega_0 f}{[1 + (f/f_0)^2]} = \frac{M_0}{4\pi\rho r\beta^3} \frac{f}{[1 + (f/f_0)^2]} \tag{A1}$$

with an assumed spectral falloff of $n = 2$. The value r represents the source station distance, β represents the shear wave speed, and ρ the density.

Calculating the integrated velocity I assuming an ideal case of an unlimited bandwidth (i.e., integrating from 0 to infinite frequency),

$$I = \int_{-\infty}^{\infty} \hat{u}^2(\omega)\mathrm{d}\omega = \frac{M_0^2}{2\rho^2\beta^6 r^2} \int_0^{\infty} \frac{f^2}{[1 + (f/f_0)^2]^2}\mathrm{d}f \tag{A2}$$

$$I = \frac{M_0^2}{2\rho^2\beta^6 r^2} f_0^4 \left[\frac{\arctan(f/f_0)}{2f_0} - \frac{f}{2(f_0^2 + f^2)} \right]\Bigg|_0^{\infty}. \tag{A3}$$

If we define $F(f, f_0)$ as follows,

$$F(f, f_0) \equiv \frac{-f/f_0}{1 + (f/f_0)^2} + \arctan(f/f_0), \tag{A4}$$

then

$$I = \frac{M_0^2}{2\rho^2\beta^6 r^2} f_0^3 F(f, f_0)\Big|_0^{\infty} = \frac{M_0^2}{4\rho^2\beta^6 r^2} f_0^3 (\frac{\pi}{2} + 0), \tag{A5}$$

$$I = \frac{\pi}{8\rho^2\beta^6 r^2} M_0^2 f_0^3. \tag{A6}$$

The radiated seismic energy (E_R) in terms of I is then given by

$$E_R = \langle U_{\theta\phi}^2 \rangle 4\pi\rho\beta r^2 I, \tag{A7}$$

where $\langle U_{\theta\phi}^2 \rangle = 2/5$ is the mean S wave radiation pattern over the focal sphere, β is the S wave velocity, ρ is the rock density, r is the source-receiver distance, and I is a definite integral given by equation (A6) [*Abercrombie*, 1995; *Boatwright and Fletcher*, 1984; *Aki and Richards*, 2002].

Substituting the expression in equation (A6) into equation (A7) leads to the analytical expression for radiated energy in terms of moment and corner frequency given by equation (9)

$$E_R = \frac{\pi^2}{5\rho\beta^5} M_0^2 f_0^3. \quad \text{(A8)}$$

Acknowledgments

We would like to thank those responsible for the instrument installation and data collection at Mount St. Helens in September 2006. In particular, we would like to thank the USGS Cascades Volcano Observatory for providing helicopter support and personnel for the experiment, as well equipment for four of the temporary stations. We also thank the IRIS PASSCAL program for loan of equipment used at three of our sites, the USGS Volcano Disaster Assistance Program for loan of equipment for two stations, and Emily Brodsky for the loan of equipment for one station. Additional data from the permanent Pacific Northwest Seismic Network was used for event locations. All data used in the analysis are available on the Incorporated Research Institutions for Seismology (IRIS) website (http://www.iris.edu/hq/) or upon request from the Cascades Volcano Observatory. R.M. Harrington was supported by a fellowship from the Alexander von Humboldt Foundation, as well as funding from the "Concept for the Future" of the Karlsruhe Institute of Technology (KIT) within the framework of the national "Initiative for Excellence" for a portion of this work. G. Kwiatek acknowledges financial support from the EU-GEISER FP7 project (http://www.geiser-fp7.eu).

References

Abercrombie, R. E. (1995), Earthquake source scaling relationships from -1 to 5 M(L) using seismograms recorded at 2.5-km depth, *J. Geophys. Res.*, *100*, 24,015–24,036.

Abercrombie, R. E., and J. R. Rice (2005), Can observations of earthquake scaling constrain slip weakening?, *Geophys. J. Int.*, *162*, 406–424.

Aki, K. (1967), Scaling law of seismic spectrum, *J. Geophys. Res.*, *72*, 1217–1231.

Aki, K., and P. G. Richards (2002), *Quantitative Seismology*, 2nd ed., Univ. Sci., Sausalito, Calif.

Aki, K., M. Fehler, and S. Das (1977), Source mechanism of volcanic tremor: Fluid-driven crack models and their application to the 1963 Kilauea eruption, *J. Volcanol. Geotherm. Res.*, *2*, 259–287.

Allmann, B. P., and P. M. Shearer (2007), Spatial and temporal stress drop variations in small earthquakes near Parkfield, California, *J. Geophys. Res.*, *112*, B04305, doi:10.1029/2006JB004395.

Anderson, J. G. (1986), Implication of attenuation for studies of the earthquake source, in *Earthquake Source Mechanics*, *Geophys. Monogr. Ser.*, vol. 37, pp. 311–318, AGU, Washington, D. C.

Baltay, A., S. Ide, G. Prieto, and G. C. Beroza (2011), Variability in earthquake stress drop and apparent stress, *Geophys. Res. Lett.*, *38*, L06303, doi:10.1029/2011GL046698.

Bean, C., I. Lokmer, and G. O'Brien (2008), Influence of near-surface volcanic structure on long-period siesmic signals and on moment tensor inversions: Simulated examples from Mount Etna, *J. Geophys. Res.*, *113*, B08308, doi:10.1029/2007JB005468.

Bean, C. J., L. De Barros, I. Lokmer, J. P. Métaxian, G. O'Brien, and S. Murphy (2014), Long-period seismicity in the shallow volcanic edifice formed from slow-rupture earthquakes, *Nat. Geosci.*, *7*, 71–75.

Beresnev, I. A. (2002), Source parameters observable from the corner frequency of earthquake spectra, *Bull. Seismol. Soc. Am.*, *92*, 2047–2048.

Boatwright, J. (1980), Spectral theory for circular seismic sources–simple estimates of source dimension, dynamic stress drop, and radiated seismic energy, *Bull. Seismol. Soc. Am.*, *70*, 1–27.

Boatwright, J., and J. B. Fletcher (1984), The partition of radiated energy between P and S waves, *Bull. Seismol. Soc. Am.*, *74*(2), 361–376.

Boore, D. M., and J. Boatwright (1984), Average body-wave radiation coefficients, *Bull. Seismol. Soc. Am.*, *74*, 1615–1621.

Brune, J. N. (1970), Tectonic stress and the spectra of seismic shear waves from earthquakes, *J. Geophys. Res.*, *75*, 4997–5009.

Brune, J. N. (1971), Seismic sources fault plane studies and tectonics, *Eos Trans. AGU*, *52*(5), IUGG 178–IUGG 187, doi:10.1029/EO052i005pIU178.

Chouet, B. A. (1996), Long-period volcano seismicity: Its source and use in eruption forecasting, *Nature*, *380*, 309–316.

Dreger, D., R. M. Nadeau, and A. Chung (2007), Repeating earthquake finite source models: Strong asperities revealed on the San Andreas Fault, *Geophys. Res. Lett.*, *34*, L23302, doi:10.1029/2007GL031353.

Eshelby, J. D. (1957), The determination of the elastic field of an ellipsoidal inclusion, and related problems, *Proc. R. Soc. London, Ser. A*, *241*(1226), 376–396.

Foulger, G. R., B. R. Julian, D. P. Hill, A. M. Pitt, P. E. Malin, and E. Shalev (2004), Non-double-couple microearthquakes at Long Valley caldera, California, provide evidence for hydraulic fracturing, *J. Volcanol. Geotherm. Res.*, *132*, 45–71.

Freund, L. B. (1979), The mechanics of dynamic shear crack propagation, *J. Geophys. Res.*, *84*, 2199–2209.

Galluzzo, D., E. Del Pezzo, M. La Rocca, M. Castellano, and F. Bianco (2009), Source scaling and site effects at Vesuvius Volcano, *Bull. Seismol. Soc. Am.*, *99*, 1705–1719.

Gerlach, T. M., K. A. McGee, and M. P. Doukas (2008), Emissions rates of CO_2, SO_2, and h_2s, scrubbing, and preeruption excess volatiles at Mount St. Helens, 2004–2005, in *A Volcano Rekindled: The Renewed Eruption of Mount St. Helens, 2004–2006*, *U.S. Geol. Surv. Open File Rep.*, 543–572.

Goldstein, P., and B. Chouet (1994), Array measurements and modeling of sources of shallow volcanic tremor at Kilauea Volcano, Hawaii, *J. Geophys. Res.*, *99*, 2637–2652.

Goto, A. (1999), A new model for volcanic earthquake at Unzen volcano: Melt rupture model, *Geophys. Res. Lett.*, *26*, 2541–2544.

Gudmundsson, O., D. M. Finlayson, I. Itikarai, Y. Nishimura, and W. R. Johnson (2004), Seismic attenuation at Rabaul volcano, Papua New Guinea, *J. Volcanol. Geotherm. Res.*, *130*, 77–92.

Harrington, R. M., and E. E. Brodsky (2007), Volcanic hybrid earthquakes that are brittle-failure events, *Geophys. Res. Lett.*, *34*, L06308, doi:10.1029/2006GL028714.

Harrington, R. M., and E. E. Brodsky (2009), Source duration scales with magnitude differently for earthquakes on the San Andreas Fault and on secondary faults in Parkfield, Calif., *Bull. Seismol. Soc. Am.*, *99*, 2323–2334.

Haskell, N. A. (1964), Total energy and energy spectral density of elastic wave radiation from propagating faults, *Bull. Seismol. Soc. Am.*, *54*, 1181–1841.

Haskell, N. A. (1966), Total energy and energy spectral density of elastic wave radiation from propagating faults 2: A statistical source model, *Bull. Seismol. Soc. Am.*, *56*, 125–140.

Hastings, W. K. (1970), Monte Carlo sampling methods using Markov chains and their applications, *Biometrica*, *57*, 97–109.

Heaton, T. H. (1990), Evidence for and implications of self-healing pulses of slip in earthquake rupture, *Phys. Earth Planet. Inter.*, *64*, 1–20.

Herriott, T. M., D. R. Sherrod, J. S. Pallister, and J. W. Vallance (2008), A volcano rekindled: The renewed eruption of Mount St. Helens, 2004-2006, *U.S. Geol. Surv. Prof. Pap., 1750*, chap. 10, 209–224.

Ide, S., and G. C. Beroza (2001), Does apparent stress vary with earthquake size?, *Geophys. Res. Lett.*, *28*, 3349–3352.

Ide, S., G. C. Beroza, S. G. Prejean, and W. L. Ellsworth (2003), Apparent break in earthquake scaling due to path and site effects on deep borehole recordings, *J. Geophys. Res.*, *108*(B5), 2271, doi:10.1029/2001JB001617.

Imanishi, K., and W. L. Ellsworth (2006), Source scaling relationships of microearthquakes at Parkfield, CA, determined using the SAFOD pilot hole seismic array, in *Earthquakes: Radiated Energy and the Physics of Faulting*, *Geophys. Monogr. Ser.*, edited by R. E. Abercrombie et al., pp. 81–90, AGU, Washington, D. C.

Imanishi, K., M. Takeo, W. L. Ellsworth, H. Ito, T. Matsuzawa, Y. Kuwahara, Y. Iio, S. Horiuchi, and S. Ohmi (2004), Source parameters and rupture velocities of microearthquakes in Western Nagano, Japan, determined using stopping phases, *Bull. Seismol. Soc. Am.*, *94*, 1762–1780.

Iverson, R. M., et al. (2006), Dynamics of seismogenic volcanic extrusion at Mount St. Helens in 2004-05, *Nature*, *444*, 439–443.
Julian, B. R. (1994), Volcanic tremor—Nonlinear excitation by fluid-flow, *J. Geophys. Res.*, *99*, 11,859–11,877.
Kanamori, H., and E. E. Brodsky (2004), The physics of earthquakes, *Rep. Prog. Phys.*, *67*, 1429–1496.
Kedar, S., B. Sturtevant, and H. Kanamori (1996), The origin of harmonic tremor at Old Faithful geyser, *Nature*, *379*, 708–711.
Kennedy, L. A., J. K. Russell, and E. Nelles (2009), Origins of Mount St. Helens cataclasites: Experimental insights, *Am. Mineral.*, *94*, 995–1004.
Kwiatek, G., K. Plenkers, and G. Dresen (2011), Source parameters of picoseismicity recorded at Mponeng deep gold mine, South Africa: Implications for scaling relations, *Bull. Seismol. Soc. Am.*, *101*, 2592–2608.
Kwiatek, G., F. Bulut, M. Bohnhoff, and G. Dresen (2014), High-resolution analysis of seismicity induced at Berlín geothermal field, El Salvador, *Geothermics*, *52*, 98–111.
Lacruz, J., A. Ugalde, C. A. Vargas, and E. Carcole (2009), Coda-wave attenuation imaging of Galeras volcano, Columbia, *Bull. Seismol. Soc. Am.*, *99*, 3510–3515.
Lahr, J. (1999), Hypoellipse: a computer program for determining local earthquake hypcentral parameters, magnitude, and first-motion pattern, *U. S. Geol. Surv. Open File Rep., 99-23*, 119 pp.
Madariaga, R. (1976), Dynamics of an expanding circular fault, *Bull. Seismol. Soc. Am.*, *66*, 639–666.
Malone, S. D. (1983), Volcanic earthquakes: Examples from Mount St. Helens, in *Earthquakes: Observations, Theory, and Interpretion*, pp. 436–455, Societa Italiana di Fisica, Bolgna.
Matoza, R. S., and B. A. Chouet (2010), Subevents of long-period seismicity: Implications for hydrothermal dynamics during the 2004–2008 eruption of Mount St. Helens, *J. Geophys. Res.*, *115*, B12206, doi:10.1029/2010JB007839.
Matoza, R. S., M. A. Garces, B. A. Chouet, L. D'Auria, M. Hedlin, C. De Groot-Hedlin, and G. P. Waite (2009), The source of infrasound associated with long-period events at Mount St. Helens, *J. Geophys. Res.*, *114*, B04305, doi:10.1029/2008JB006128.
Metropolis, N., A. Rosenbluth, M. Rosenbluth, A. Teller, and E. Teller (1953), Equation of state calculations by fast computing machines, *J. Chem. Phys.*, *21*, 1087–1092.
Moran, S. C., S. D. Malone, A. I. Qamar, W. A. Thelen, A. K. Wright, and J. Caplan-Auerbach (2008a), Seismicity associated with renewed dome building at Mount St. Helens, 2004-2005: Chapter 2, in *A Volcano Rekindled: The Renewed Eruption of Mount St. Helens, 2004-2006*, *U.S. Geol. Surv. Prof. Pap., 1750–2*, 27–60.
Moran, S. C., P. J. McChesney, and A. B. Lockhart (2008b), Seismicity and infrasound associated with explosions at Mount St. Helens, 2004–2005: Chapter 6, in *A Volcano Rekindled: The Renewed Eruption of Mount St. Helens, 2004-2006*, *U.S. Geol. Surv. Prof. Pap., 1750–6*, 111–127.
Mosegaard, K., and A. Tarantola (1995), Monte Carlo sampling of solutions to inverse problems, *J. Geophys. Res.*, *100*(12), 12,431–12,447.
Neuberg, J. W. (2000), Characteristics and causes of shallow seismicity in andesite volcanoes, *Philos. Trans. R. Soc. London, Ser. A*, *358*, 1533–1546.
Pallister, J. S., K. V. Cashman, J. T. Hagstrum, N. M. Beeler, S. C. Moran, and R. P. Denlinger (2013), Faulting within the Mount St. Helens conduit and implications for volanic earthquakes, *Geol. Soc. Am. Bull.*, *125*, 359–376.
Petrosino, S., P. Cusano, G. Saccorotti, and E. Del Pezzo (2002), Seismic attenuation of shallow velocity structures at Stromboli volcano, Italy, *Bull. Seismol. Soc. Am.*, *92*, 1102–1116.
Prejean, S. G., and W. L. Ellsworth (2001), Observations of earthquake source parameters at 2 km depth in the Long Valley caldera, eastern California, *Bull. Seismol. Soc. Am.*, *91*, 165–177.
Prieto, G. A., P. M. Shearer, F. L. Vernon, and D. Kilb (2004), Earthquake source scaling and self-similarity estimation from stacking P and S spectra, *J. Geophys. Res.*, *109*, B08310, doi:10.1029/2004JB003084.
Rust, A., N. Balmforth, and S. Mandre (2008), The feasibility of generating low-frequency volcano seismicity by flow through a deformable channel, *Geol. Soc. London Spec. Publ.*, *307*, 45–56.
Saccorotti, G., I. Lokmer, C. J. Bean, G. Di Grazia, and D. Patane (2007), Analysis of sustained long-period activity at Etna Volcano, Italy, *J. Volcanol. Geotherm. Res.*, *160*, 340–354.
Scott, W. E., D. R. Sherrod, and C. A. Garnder (2008), Overview of the 2004 to 2006, and continuing, eruption of Mount St. Helens, Washington, in *A Volcano Rekindled: The Renewed Eruption of Mount St. Helens*, *2004-2006*, *U.S. Geol. Surv. Open File Rep.*, 3–22.
Shearer, P. M., G. A. Prieto, and E. Hauksson (2006), Comprehensive analysis of earthquake source spectra in southern California, *J. Geophys. Res.*, *111*, B06303, doi:10.1029/2005JB003979.
Snoke, J. A. (1987), Stable determination of (Brune) stress drops, *Bull. Seismol. Soc. Am.*, *77*, 530–538.
Thelen, W. A., R. S. Crosson, and K. C. Creager (2008), Absolute and relative locations of earthquake at Mount St. Helens, Washington, using continuous data: Implications for magmatic processes, *U.S. Geol. Surv. Prof. Pap., 1750*, chap. 4, 71–96.
Tomic, J., R. E. Abercrombie, and A. F. Nascimento (2006), Source parameters and rupture velocity of small $M \leq 2.1$ reservoir induced earthquakes, *Geophys. J. Int.*, *179*, 1013–1023.
Tuffen, H., R. Smith, and P. R. Sammonds (2008), Evidence for seismogenic fracture of silicic magma, *Nature*, *453*, 511–514.
Vallance, J. W., D. J. Schneider, and S. P. Schilling (2008), A volcano rekindled: The renewed eruption of Mount St. Helens, 2004–2006, *U.S. Geol. Surv. Prof. Pap., 1750*, chap. 9, 169–208.
Venkataraman, A., G. C. Beroza, and J. Boatwright (2006), A brief review of techniques used to estimate radiated seismic energy, *Geophys. Monogr.*, *170*, 15–24.
Waite, G. P., and S. C. Moran (2009), v_P structure of Mount St. Helens, Washington, USA, imaged with local earthquake tomography, *J. Volcanol. Geotherm. Res.*, *182*, 113–122.
Waite, G. P., B. A. Chouet, and P. B. Dawson (2008), Eruption dynamics at Mount St. Helens imaged from broadband seismic waveforms: Interaction of the shallow magmatic and hydrothermal systems, *J. Geophys. Res.*, *113*, B02305, doi:10.1029/2007JB005259.
Waldhauser, F. (2001), hypoDD: A computer program to compute double-difference hypocenter locations, *U.S. Geol. Surv. Open File Rep., 2001–113*, p. 25.
Waldhauser, F., and W. L. Ellsworth (2000), A double-difference earthquake location algorithm: Method and application to the northern Hayward fault, California, *Bull. Seismol. Soc. Am.*, *90*, 1353–1368.
Yamada, T., J. J. Mori, S. Ide, H. Kawakata, and Y. Iio (2005a), Radiation efficiency and apparent stress of small earthquakes in a South African gold mine, *J. Geophys. Res.*, *110*, B01305, doi:10.1029/2004JB003221.
Yamada, T., J. J. Mori, S. Ide, H. Kawakata, and Y. Iio (2005b), Correction to "Radiation efficiency and apparent stress of small earthquakes in a South African gold mine", *J. Geophys. Res.*, *110*, B06301, doi:10.1029/2005JB003789.